

Effects of pre-injection on ignition, combustion and emissions of spray under engine-like conditions

Jangi, Mehdi

DOI:

[10.1016/j.combustflame.2022.112082](https://doi.org/10.1016/j.combustflame.2022.112082)

License:

Creative Commons: Attribution (CC BY)

Document Version

Publisher's PDF, also known as Version of record

Citation for published version (Harvard):

Jangi, M 2022, 'Effects of pre-injection on ignition, combustion and emissions of spray under engine-like conditions', *Combustion and Flame*, vol. 241, 112082. <https://doi.org/10.1016/j.combustflame.2022.112082>

[Link to publication on Research at Birmingham portal](#)

General rights

Unless a licence is specified above, all rights (including copyright and moral rights) in this document are retained by the authors and/or the copyright holders. The express permission of the copyright holder must be obtained for any use of this material other than for purposes permitted by law.

- Users may freely distribute the URL that is used to identify this publication.
- Users may download and/or print one copy of the publication from the University of Birmingham research portal for the purpose of private study or non-commercial research.
- User may use extracts from the document in line with the concept of 'fair dealing' under the Copyright, Designs and Patents Act 1988 (?)
- Users may not further distribute the material nor use it for the purposes of commercial gain.

Where a licence is displayed above, please note the terms and conditions of the licence govern your use of this document.

When citing, please reference the published version.

Take down policy

While the University of Birmingham exercises care and attention in making items available there are rare occasions when an item has been uploaded in error or has been deemed to be commercially or otherwise sensitive.

If you believe that this is the case for this document, please contact UBIRA@lists.bham.ac.uk providing details and we will remove access to the work immediately and investigate.



Effects of pre-injection on ignition, combustion and emissions of spray under engine-like conditions

Ahmad Hadadpour^{a,b,*}, Shijie Xu^a, Kar Mun Pang^c, Xue-Song Bai^a, Mehdi Jangi^{d,*}

^a Division of Fluid Mechanics, Department of Energy Science, Lund University, P.O. Box 118, Lund S 221 00, Sweden

^b Scania AB, Södertälje SE-15187, Sweden

^c MAN Energy Solutions, Teglholmegade 41, Copenhagen SV 2450, Denmark

^d Department of Mechanical Engineering, School of Engineering, University of Birmingham, Birmingham B15 2TT, UK

ARTICLE INFO

Article history:

Received 29 April 2020

Revised 18 February 2022

Accepted 22 February 2022

Keywords:

Pre-injection

Eulerian stochastic field

Transported probability density function

Flamelet generated manifold

Engine combustion network

Spray-A

ABSTRACT

Large-eddy simulation (LES) of multiple-injection spray combustion under engine-like conditions is performed using a coupled model of an Eulerian stochastic field transported probability density function (ESF T-PDF) and a flamelet generated manifold (FGM). This coupled model allows the use of the T-PDF methods in modeling the interaction of turbulence and chemistry at affordable computational costs for engine applications. Simulation results are compared with the available experimental data for spray flames with multiple-injection and at a high level of exhaust gas recirculation (EGR) under conditions relevant to internal combustion engines. It is shown that the T-PDF/FGM LES model is capable of reproducing not only global combustion characteristics, such as the pressure rise and ignition delay time but also replicating the evolution of liftoff length and the spray flame structure.

The effects of pre-injection strategies are then investigated, by systematically varying the pre-injection duration and the dwell time between two injections, while keeping the total injected fuel mass constant. The LES results reveal different mechanisms by which a pre-injection can change the ignition delay time, the combustion mode and the emissions in spray flames, depending on the injection timing. It is shown that even an extremely short non-igniting pre-injection can substantially change the ignition and emissions characteristics of the main-injection. It is shown that the combustion mode of a single-injection can be altered by splitting the injection to pre- and main-injections. The current study also demonstrates that decreasing the dwell time, within the range that is examined here, at a given pre-injection, will potentially increase the soot oxidation rates while it does not significantly change the rate of soot formation.

© 2022 The Author(s). Published by Elsevier Inc. on behalf of The Combustion Institute.
This is an open access article under the CC BY license (<http://creativecommons.org/licenses/by/4.0/>)

1. Introduction

Multiple-injection strategies which split a single-injection into separate pre-, main- and/or post-injections, are commonly used to improve diesel engine performance. Recent works, however, have shown that at given operating conditions, the behavior of both NO_x and soot emissions of an engine can be improved or worsened, depending on the adopted injection splitting strategy [1–4]. For instance, there is a general agreement that a pre-injection can shorten the ignition delay time (IDT) of the main-injection and reduce NO_x, CO, and unburned hydrocarbon (UHC) emissions. However, it has been reported that the pre-injection can potentially in-

crease the soot emission of the main-injection [2,5,6], compared to that of a single-injection without splitting. It is not clear if this increase is due to the increase of soot formation process resulting from insufficient fuel/air premixing time, the shortening of the IDT, or the lower soot oxidation rate as a result of lower local flame temperature.

Such trade-offs between the desired effects of any multiple-injection strategy and their undesired side-effects must be carefully taken care of in the design of these strategies for engine applications. Generally in those designs, the large number of key controlling parameters that are involved, such as operating conditions (e.g., temperature, pressure and level of oxygen in the ambient environment), the number of split injections, the duration of each injection, the dwell time between them and the nonlinear coupling effects of these parameters, makes the optimization of an injection strategy a challenging task [7]. Indeed, the design of such

* Corresponding authors.

E-mail addresses: ahmad.hadadpour@scania.com, ahmad.hadadpour@energy.lth.se (A. Hadadpour), m.jangi@bham.ac.uk (M. Jangi).

optimized multiple-injection strategy is impossible without understanding the underlying physics of each effect.

To improve such understanding and to explain the effects of each of these parameters in multiple-injection schemes, many studies are ongoing [2,8–20]. Skeen et al. [8], investigated the ignition of n-dodecane in a double-injection and reported that the IDT for the second injection is shorter than that for the first one. They also observed a greater amount of soot in the second injection than what was observed in the first injection. They suggested that this is due to the shorter IDT and lower local oxygen concentration for the second injection. However, since they examined only one injection timing, they highlighted that this conclusion may change by varying the pre- and main-injections duration and dwell time (hereinafter pre-injection timing) and further investigations were recommended.

In a separate study on a similar case, Moiz et al. [2] reported the same observation on the shortening of IDT. To explain this effect, they suggested various potential mechanisms which can be dominant depending on the different operating conditions. Although a pre-injection prepares the mixture for a shorter IDT and faster combustion of main-injection, its heat release might reduce the efficiency of the engine. This is the case if the ignition and combustion of the pre-injection occur during the compression stroke. One way to avoid such a scenario is to advance the pre-injection to much earlier than the top-dead-center (TDC). This way, the in-cylinder gases are still at a low temperature (e.g., 750 K) and the pre-injection does not ignite before the injection and ignition of the main-injection. Such injections at a lower in-cylinder temperature condition have been examined in the mentioned experiments [2,8], and can be applied to delay the ignition of pre-injection to any time later than the start of the main-injection. This strategy in an engine, however, can lead to over-dilution from the pre-injection due to long dwell time, hence it can increase the UHC emissions and potentially reduce the efficiency of the engine [21]. Accordingly, it is highly desirable to optimize pre-injection timing in a way that it does not ignite, hence, does not release significant heat before the ignition of the main-injection. In this sense, the fuel from pre-injection is desired to be partially oxidized and act as an ignition precursor for the main-injection.

Set against these backgrounds, in the current study, we use large-eddy simulation (LES) to explain the underlying physics of the two explained potential side-effects of pre-injection, i.e., the increase of soot and the heat release before the start of the main-injection. For this purpose, LES is highly desirable as it can provide information about the local chemical composition and temperature in such detail that is required to fully understand the process in the system. We first investigate the mechanisms by which the pre-injection timing changes the ignition, combustion and emission of the main-injection. Subsequently, we systematically change the duration of pre-injection and dwell time to examine the validity and importance of the suggested mechanisms in various pre-injection timings with identical operating conditions. Based on this understanding, we strive to propose a method to reduce the mentioned side-effects only by modifying the pre-injection timing.

The originality of this work lies in that (1) for the first time we use a hybrid Flamelet-generated manifold (FGM)/Eulerian stochastic fields, which we have recently developed for modeling multiple-injection combustion in an accurate and computationally affordable manner; (2) we introduce a new reaction progress variable (RPV) using local oxygen consumption and assess its performance compared with a commonly-used RPV; (3) based on the validated simulation results, we suggest mechanisms that a pre-injection can affect the IDT, combustion mode and soot emissions in the main-injection, and we discuss the dominant mechanism for

Table 1

Some of the recent LES studies of ECN spray cases. n-dodecane and n-heptane are used as fuel in Spray-A and Spray-H, respectively.

| Fuel | Species number | TCI* model | Minimum cell size [μm] | Ref. |
|-----------------------|----------------|------------|-------------------------------------|------|
| n-heptane | 42, 68 | WSR | 125 | [22] |
| n-dodecane | 103 | WSR | 250 | [23] |
| n-heptane | 44 | FMDf | 200 | [24] |
| n-dodecane | 103 | WSR | 62.5 | [25] |
| n-dodecane | 257, 103 | FGM | 62.5 | [26] |
| n-heptane | 22 | ESF | 500 | [27] |
| n-dodecane | 54 | CMC | 62.5 | [19] |
| n-dodecane | 103 | TFM | 62.5 | [28] |
| n-heptane | 140 | WSR | 62.5 | [29] |
| n-dodecane | 54 | PaSR | 240 | [11] |
| n-dodecane | 54, 96 | WSR | 62.5 | [30] |
| n-dodecane | 54 | WSR | 62.5 | [31] |
| n-dodecane | 54–255 | WSR | 62.5 | [32] |
| n-heptane | 68 | ESF | 250 | [33] |
| n-heptane | 68 | FGM | 250 | [34] |
| n-dodecane | 54 | PaSR | 250 | [35] |
| n-heptane | 68 | ESF | 250 | [36] |
| n-heptane | 68 | ESF | 250 | [37] |
| n-dodecane | 54 | WSR | 125 | [38] |
| n-dodecane, n-heptane | 57, 130, 257 | PaSR | 125 | [39] |
| n-heptane | 68 | PaSR | 125 | [40] |

various pre-injection timing; (4) we show that how a very short non-ignition pre-injection can modify the IDT of main-injection by changing the local distribution of reacting species.

In this work, Spray-A case from Engine Combustion Network (ECN), which is designed to mimic spray combustion in engines, is simulated. The ECN spray flames have been widely studied experimentally and numerically, therefore a good database is available for the performance assessment of the simulation. Some of the recent numerical studies of ECN spray combustion cases, including Spray-A and Spray-H, are listed in Table 1. The Spray-A and Spray-H cases use n-dodecane and n-heptane, respectively, as fuel.

* TCI: Turbulence-Chemistry Interaction, WSR: Well Stirred Reactor, FMDf: Filtered Mass Density Function, FGM: Flamelet Generated Manifold, ESF: Eulerian Stochastic Field, CMC: Conditional Moment Closure, TFM: Tabulated Flamelet Model, PaSR: Partially Stirred Reactor.

2. Numerical method

2.1. Large eddy simulation of the flow

An LES is applied for the gaseous phase by solving the Favre-filtered conservation equations of mass and momentum, which can be written as:

$$\frac{\partial \bar{\rho}}{\partial t} + \frac{\partial \bar{\rho} \tilde{u}_j}{\partial x_j} = \bar{S}_\rho, \quad (1)$$

$$\frac{\partial \bar{\rho} \tilde{u}_i}{\partial t} + \frac{\partial}{\partial x_j} (\bar{\rho} \tilde{u}_i \tilde{u}_j - \bar{\tau}_{ij} - \tau_{ij}^{sgs}) = \bar{S}_{u_i}, \quad (2)$$

where the overline denotes the general filtering and tilde denotes the Favre filtering; u_i is velocity component along x_i -direction; ρ is density; \bar{S}_ρ and \bar{S}_{u_i} are spray source terms that account for the exchange rate of the mass and momentum, respectively, between the gas and liquid phases; $\bar{\tau}_{ij}$ is filtered viscous stress tensor obtained from the resolved strained rate and τ_{ij}^{sgs} is subgrid stress tensor.

2.2. Tabulated chemistry method

For the simulation of combustion, an FGM approach is applied, in which the mass fraction of species as well as reaction source

terms are tabulated in terms of mixture fraction (Z) and RPV (\mathcal{Y}). In FGM modeling of spray combustion, cooling effects of liquid fuel evaporation must be taken into account for the calculation of temperature (T). To perform this calculation, an approach, which is discussed and validated in Ref. [26], is adopted. In this approach, the transport equation for sensible enthalpy, h , is solved separately in the simulations. The temperature is then evaluated based on the calculated enthalpy and mass fraction of species. Since the h equation includes a spray source term, the energy exchange between the liquid and the gas phase, hence, the associated cooling effects of spray evaporation are taken into account in the calculation of temperature. The evaporation mainly affects the temperature in the liquid spray region, and its effect is expected to be milder downstream of this region where the ignition and majority of reactions take place. Although this effect on the species mass fraction could also be modeled by varying fuel-side temperature in the FGM tables at the cost of adding an additional table entry, Ref. [26] demonstrated that the final results in the case of this study are almost insensitive to such change of the fuel-side temperature.

2.3. Turbulence-chemistry interaction

To accurately model the turbulence-chemistry interaction (TCI) in the present work, instead of presuming a PDF shape of Z and \mathcal{Y} , the Eulerian stochastic fields (ESF) transported probability density function (T-PDF) method is applied. The transport equation of the joint sub-grid scales (SGS) PDF is solved with the Monte Carlo method [41]. In this approach, the joint PDF is estimated by an ensemble of N_{SF} stochastic fields (where N_{SF} is the number of stochastic fields).

The stochastic differential equations (SDE) for the n^{th} stochastic field of Z , \mathcal{Y} and h are written as:

$$\begin{aligned} \bar{\rho} dZ^{(n)} = & -\bar{\rho} \tilde{u}_i \frac{\partial Z^{(n)}}{\partial x_i} dt + \frac{\partial}{\partial x_i} (\Gamma_t \frac{\partial Z^{(n)}}{\partial x_i}) dt \\ & - \frac{1}{2} \bar{\rho} C_\phi (Z^{(n)} - \tilde{Z}) \omega^{sgs} dt + \bar{\rho} \sqrt{2 \frac{\Gamma_t}{\bar{\rho}}} \frac{\partial Z^{(n)}}{\partial x_i} d\mathbf{W}_i^{(n)} \\ & + \bar{S}_Z^{(n)} dt, \end{aligned} \quad (3)$$

$$\begin{aligned} \bar{\rho} d\mathcal{Y}^{(n)} = & -\bar{\rho} \tilde{u}_i \frac{\partial \mathcal{Y}^{(n)}}{\partial x_i} dt + \frac{\partial}{\partial x_i} (\Gamma_t \frac{\partial \mathcal{Y}^{(n)}}{\partial x_i}) dt \\ & - \frac{1}{2} \bar{\rho} C_\phi (\mathcal{Y}^{(n)} - \tilde{\mathcal{Y}}) \omega^{sgs} dt + \bar{\rho} \sqrt{2 \frac{\Gamma_t}{\bar{\rho}}} \frac{\partial \mathcal{Y}^{(n)}}{\partial x_i} d\mathbf{W}_i^{(n)} \\ & + \bar{\rho} S_Y^{(n)} (Z^{(n)}, \mathcal{Y}^{(n)}) dt, \end{aligned} \quad (4)$$

$$\begin{aligned} \bar{\rho} dh^{(n)} = & dp - \bar{\rho} \tilde{u}_i \frac{\partial h^{(n)}}{\partial x_i} dt + \frac{\partial}{\partial x_i} (\Gamma_t \frac{\partial h^{(n)}}{\partial x_i}) dt \\ & - \frac{1}{2} \bar{\rho} C_\phi (h^{(n)} - \tilde{h}) \omega^{sgs} dt + \bar{\rho} \sqrt{2 \frac{\Gamma_t}{\bar{\rho}}} \frac{\partial h^{(n)}}{\partial x_i} d\mathbf{W}_i^{(n)} \\ & + \bar{\rho} S_h^{(n)} (Z^{(n)}, \mathcal{Y}^{(n)}) dt + \bar{S}_h^{(n)} dt, \end{aligned} \quad (5)$$

with $n = 1, 2, \dots, N_{SF}$. These equations imply invoking the gradient-transport hypothesis for approximating the SGS turbulent transport. $\Gamma_t = \frac{\mu}{\sigma} + \frac{\mu^{sgs}}{\sigma^{sgs}}$ is the sum of molecular plus SGS diffusivity. The terms involve C_ϕ , where $C_\phi = 2$ [42], is the micro-mixing modeled by the Interaction with Exchange to the Mean (IEM) model [43]. In these terms, ω^{sgs} is SGS turbulent frequency modeled as $\omega^{sgs} = \frac{\mu + \mu^{sgs}}{\bar{\rho} \Delta^2}$, with Δ being the filter width. The term $d\mathbf{W}_i^{(n)}$ represents a vector Wiener process that is spatially uniform but different for each field. Here $d\mathbf{W}_i^{(n)}$ is approximated by time-step increment $\sqrt{\Delta t} \eta^{(n)}$ and $\eta^{(n)}$ is a $\{-1, 1\}$ dichotomic random vector [41].

In Eqs. (3) and (5), $\bar{S}_Z^{(n)}$ and $\bar{S}_h^{(n)}$ are spray source terms for the exchange of mass and energy, respectively, with the liquid phase. The closure for these source terms are obtained using the LPT method (see Section 2.5). In Eqs. (4) and (5), $S_Y^{(n)}(Z^{(n)}, \mathcal{Y}^{(n)})$ and $S_h^{(n)}(Z^{(n)}, \mathcal{Y}^{(n)})$ are reaction source terms of the progress variable and chemical heat release rate, respectively, for the n^{th} stochastic field. These reaction source terms as well as mass fraction of species, $Y_\alpha^{(n)}(Z^{(n)}, \mathcal{Y}^{(n)})$ (α refers to different species), are computed from the looked-up FGM table using $Z^{(n)}$ and $\mathcal{Y}^{(n)}$. The n^{th} stochastic field of temperatures, $T^{(n)}$, is calculated using $h^{(n)}$ and $Y_\alpha^{(n)}$. It should be noted that no integration using a presumed PDF (e.g., β -function) in the tabulated variables is needed. Instead, using the transported joint PDF, the mean and moments of each variable are calculated from the ensemble of N_{SF} notional fields. We use $N_{SF} = 8$, which has been shown to be sufficient for the ESF method [44]. To assure this sufficiency, we examine the sensitivity of results to the number of stochastic fields by performing three simulations with $N_{SF} = 4, 8$ and 16 (see Section 4.1.2).

2.4. Flamelet generated manifold database

The FGM database is generated from the numerical solution of steady and unsteady flamelet equations for counterflow diffusion flames in mixture fraction space. These equations are solved using FlameMaster [45]. Following Ref. [26], the boundary conditions of temperature and mass fractions in the flamelet equations are set as the same values as in the experiment (see Section 3). For the generation of FGM database, 47 steady-state flamelets, ($2 \times 10^{-5} < \chi < 30 \text{ s}^{-1}$, where χ is scalar dissipation rate at stoichiometric mixture fraction), and 429 unsteady flamelets ($\chi = 30 \text{ s}^{-1}$, $0 < \tau < \infty$, where τ is the time from the unburned condition) are used. The $\chi = 30 \text{ s}^{-1}$ for the unsteady flamelets, which represent the ignition process, is chosen based on a one-dimensional analysis. The χ values ranging from 1 to 40 s^{-1} were examined in the flamelet calculations and the one that exhibited the closest IDT in the one-dimensional analysis to the reported value for n-dodecane ignition was chosen.

Three RPVs (\mathcal{Y}_{1-3}) are examined in this work as defined in the following. In the definitions of RPVs, Y_α is the mass fraction of species α and M_α is the associated molecular mass. In these definitions, to exclude the contribution of the initial gases from the definition of progress variables, a new variable is introduced and used as $Y_\alpha^* = Y_\alpha - Y_{N_2} (Y_\alpha^0 / Y_{N_2}^0)$, where Y_α^0 is the initial mass fraction of species α (see Section 3).

The first RPV is a commonly used progress variable [26], $\mathcal{Y}_1 = Y_{CO}^* / M_{CO} + Y_{CH_2O}^* / M_{CH_2O} + Y_{CO_2}^* / M_{CO_2}$. This progress variable can predict ignition and the early part of combustion reasonably well, but it does not increase monotonically after ignition [26]; hence, it cannot predict the total released heat and pressure rise correctly. To examine and confirm this, in addition to \mathcal{Y}_1 , two other RPVs are proposed in this study. The second RPV, which is also the baseline RPV in this work, is defined as $\mathcal{Y}_2 = -Y_{O_2}^* = -Y_{O_2} + Y_{N_2} (Y_{O_2}^0 / Y_{N_2}^0)$. It was observed that \mathcal{Y}_2 increases monotonically for unsteady flamelets. The third RPV is $\mathcal{Y}_3 = \sum_{\alpha=1}^{N_s} w_\alpha Y_\alpha$, where w_α is calculated using an optimization algorithm [46] involving all the species in the mixture to achieve a monotonic increase of \mathcal{Y}_3 across the flamelets. The four largest terms of \mathcal{Y}_3 are, $-6.85 \times 10^{-1} Y_{O_2}^* + 1.66 \times 10^{-1} Y_{CO_2}^* + 1.45 \times 10^{-1} Y_{CO}^* - 4.68 \times 10^{-4} Y_{C_7H_{14}}^*$. This optimized RPV in this work is used only for comparison purposes. The results of the new progress variable, \mathcal{Y}_2 , will be compared with the optimized RPV, \mathcal{Y}_3 , in addition to the comparison with the experimental measurements.

2.5. Liquid-phase spray modeling

Closures for spray source terms in Eqs. (1), (2), (3) and (5) (i.e., $\overline{S_\rho}$, $\overline{S_{u_i}}$, $\overline{S_z}$ and $\overline{S_h}$) are obtained by simulation of the liquid phase using the Lagrangian particle tracking (LPT) method. The droplets are injected with a Rosin Rammler distribution, ranging from 1 μm to the diameter of injector, 90 μm , and their break-up is modeled using the Kelvin-Helmholtz Rayleigh Taylor (KHRT) model [47]. A stochastic dispersion model is applied for the droplets dispersion. LPT uses the mean field value of temperature, and the spray source terms are added equally to each stochastic field equations (see Eqs. (3) and (5)). For more details on the spray modeling, readers are referred to our previous works [23,48].

2.6. Soot formation and oxidation

A phenomenological multi-step soot model [49] is employed to simulate the soot evolution process. In this model, the soot particle nuclei are formed from soot precursor. Upon the formation of the soot nuclei, they subsequently undergo surface growth, coagulation and oxidation. Eqs. (6) and (7) are the governing equations for particle number density, ϕ_N , and soot mass fraction, Y_{soot} .

$$\frac{\partial \bar{\rho} \tilde{\phi}_N}{\partial t} + \frac{\partial \bar{\rho} \tilde{u}_j \tilde{\phi}_N}{\partial x_j} - \frac{\partial}{\partial x_j} \left(\bar{\rho} D_t \frac{\partial \tilde{\phi}_N}{\partial x_j} \right) = \frac{1}{N_A} \frac{dN}{dt}, \quad (6)$$

$$\frac{\partial \bar{\rho} \tilde{Y}_{\text{soot}}}{\partial t} + \frac{\partial \bar{\rho} \tilde{u}_j \tilde{Y}_{\text{soot}}}{\partial x_j} - \frac{\partial}{\partial x_j} \left(\bar{\rho} D_t \frac{\partial \tilde{Y}_{\text{soot}}}{\partial x_j} \right) = \frac{dM}{dt}, \quad (7)$$

in which, D_t and N_A are total diffusion coefficient and the Avogadro number, respectively. dN/dt and dM/dt are the source terms of particle number density and soot mass, respectively, which are modeled using the rates of nucleation, coagulation, surface growth and oxidation. For more details on the soot modeling, readers are referred to our previous work [49].

2.7. The solution procedure

The solution procedure at each time step is summarized as follows:

- (1) Equations of mass, momentum, mixture fraction, reaction progress variable, enthalpy and LPT are solved numerically using the conventional control volume method. These include $3 \times N_{SF}$ stochastic fields equations.
- (2) To solve Eqs. ((4)–(5)), the reaction source terms, i.e., $S_y^{(n)}(Z^{(n)}, \gamma^{(n)})$ and $S_h^{(n)}(Z^{(n)}, \gamma^{(n)})$ are required. These source terms as well as $Y_\alpha^{(n)}$ are obtained from the FGM tables, using $Z^{(n)}$ and $\gamma^{(n)}$.
- (3) The density, temperature and other thermodynamic properties of each stochastic field are calculated using $Y_\alpha^{(n)}$ and $h^{(n)}$.
- (4) The mean value of mass fraction of species, temperature, heat release rate, mixture fraction and other variables are then calculated, e.g., $\bar{Y}_\alpha = \frac{1}{N_{SF}} \sum_{n=1}^{N_{SF}} Y_\alpha^{(n)}$ and $\bar{T} = \frac{1}{N_{SF}} \sum_{n=1}^{N_{SF}} T^{(n)}$.
- (5) Soot transport equations are solved using the mean values.

The method is implemented in OpenFOAM [50]. The solution procedure includes momentum predictor, pressure solver and the momentum corrector, sequentially. Second-order discretization schemes for both time and space are employed. For the LES, the mesh size is 0.125 mm within the first 20 mm (axial) of the injector and then it is increased to 0.25 mm for the rest of the domain. In addition to the analysis of mesh size in our previous works [48,51], the sufficiency of the used mesh in resolving the required fraction of turbulence is examined in Appendix A. It should

Table 2

Specifications of injection timings in the studied cases. Double injection cases are named as P_iD_j, where subscripts of P and D in each case name refer to the duration of Pre-injection and Dwell time in that case, respectively, as specified in the table. Cases 1, 2 and 3 are the ECN cases with available experimental measurements [53].

| | Case name | Pre-injection (ms) | Dwell time (ms) | Main-injection (ms) |
|---|-------------------------------|--------------------|-----------------|---------------------|
| 1 | non-reacting | | | 1.5 |
| 2 | single-injection | | | 1.5 |
| 3 | P ₃ D ₅ | 0.3 | 0.5 | 1.2 |
| 4 | P ₃ D ₃ | 0.3 | 0.3 | 1.2 |
| 5 | P ₂ D ₃ | 0.2 | 0.3 | 1.3 |
| 6 | P ₁ D ₃ | 0.1 | 0.3 | 1.4 |

be noted that there is no general agreement in the literature on the required minimum grid size of spray cases. As can be seen in Table 1, different studies reported different grid sizes depending on the applied LPT sub-models and the implemented TCI model.

In the current simulations, a time step of $\Delta t = 20$ ns is used, which keeps the maximum Courant number below 0.1. A chemical kinetic mechanism, which consists of 130 species and 2323 reactions [52], is used in this study.

3. Case specification

As aforementioned, the Spray-A case from ECN [53], which mimics diesel spray combustion in engines, is simulated. We use measurements from three experimental cases (two reacting cases [2,54] and one non-reacting case [55]) for model validation (see Table 2). All cases involve an injection of liquid n-dodecane at 363 K through a nozzle with a diameter of 90 μm . The fuel is injected into a pressurized preheated cubical constant-volume vessel (with each side length of 108 mm). All cases have an ambient temperature of 900 K and an ambient density of 22.8 kg/m^3 . In the reacting cases, the volumetric concentration of oxygen, carbon dioxide, water vapor and nitrogen are 15%, 6.22%, 3.62% and 75.15%, respectively. These values mimic diesel engines with exhaust gas recirculation (EGR). In the non-reacting case, these volumetric concentrations are set to 0%, 6.52%, 3.77% and 89.71%, respectively [53].

In terms of injection timing, the standard Spray-A case, which has a single-injection with a duration of 1.5 ms [54], is chosen as one of the reacting baseline cases (case “single-injection” in Table 2). This case is chosen because it has been widely studied numerically and experimentally [11,25,28,31,42,54,56–73], hence results from the literature are available to evaluate the quality of the current simulation. As the second reacting validation case, a less-studied double-injection experiment [2] is considered (case P₃D₅ in Table 2). This double-injection case has a 0.3 ms duration of pre-injection and a 1.2 ms duration of main-injection. The interval time between two injections (dwell time) is 0.5 ms.

In addition to the described validation cases, three pre-injection reacting cases, which are listed in Table 2, are studied. These cases with two different dwell times and three different pre-injection timings are considered to elucidate the impact of injection strategies on diesel combustion. In all cases, a total amount of 3.46 mg fuel mass is injected. The injection mass-flow-rate profiles are adopted from ECN [53]. The adopted profiles take into account the opening and closing times of the injector. Therefore, the injected mass in each stroke of injection is not linearly proportional to its injection duration.

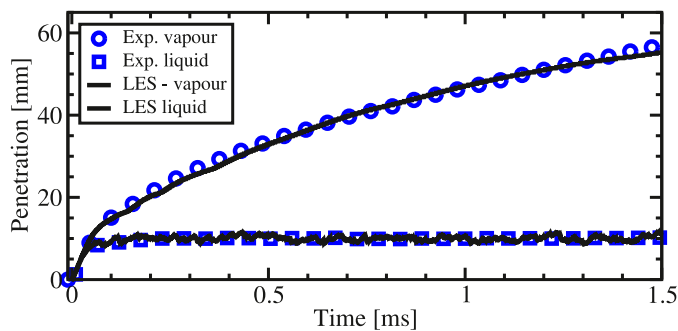


Fig. 1. The liquid and vapor penetration length for the non-reacting spray case in the LES and experiment [53,55].

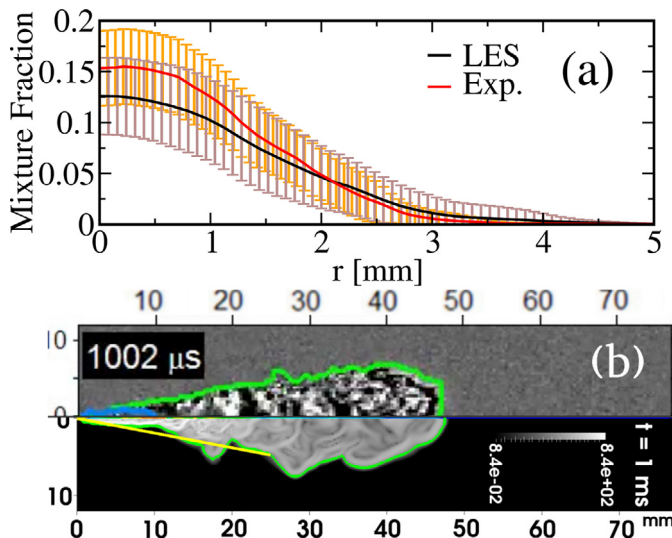


Fig. 2. (a) The radial profile and RMS of vapor mixture fraction for the non-reacting case at the axial location of 200d. (b) The Schlieren image (upper half) [53,55,74] and the LES predicted gradient of density in logarithmic scale (lower half); the green line in the LES result is isocontour of $Z = 0.001$; the yellow line is the reported cone angle (21.5°) in the experiment [74], shown for comparison.

4. Results and discussions

4.1. Model validation

4.1.1. Non-reacting spray

The present LES model is capable of replicating reasonably well the measured liquid length, vapor penetration length, the radial profile of mixture fraction, spray cone angle as well as the general structure of the spray. Fig. 1 shows the liquid and vapor penetration lengths of the non-reacting spray in the LES, which agree very well with the experiment. Following the ECN recommendation [53], the mixture fraction of 0.001 is considered as a threshold for calculation of vapor penetration in the LES. The liquid length is calculated by considering the shortest axial distance from the injector in which 95% of liquid exists.

An acceptable agreement has also been observed between the experiment and simulation in terms of the radial profile of the distribution of the vapor fuel mixture fraction for the non-reacting case. Fig. 2a shows these profiles at the axial location of 200d (d is the nozzle diameter), for the experiment and LES. The vertical bars are the root mean square (RMS) of the fluctuation of mixture fraction. Although the peak of the profile is being slightly under-predicted in the LES, the RMS values in the experiment and LES overlap fairly well. Nonetheless, this profile falls within the reported uncertainty range of the experiment.

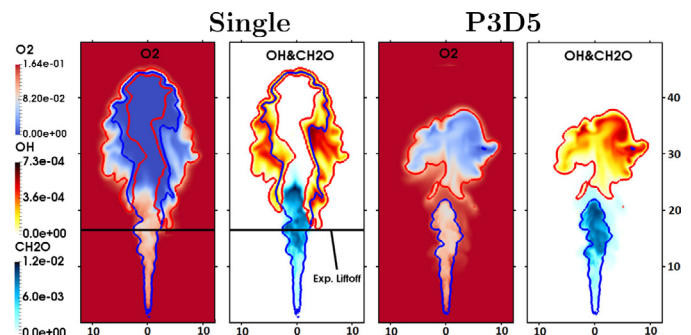


Fig. 3. Two-dimensional snapshots of the mass fraction of CH_2O , OH , and O_2 at $t = 1$ ms for the single-injection and P_3D_5 cases. The red line is the isocontour of $Y_{\text{OH}} = 1.6 \times 10^{-5}$; the blue line is the isocontour of equivalence ratio $\phi = 1$. The experimental LOL [53] is also shown with black line for comparison purposes.

To compare the structure of vapor distribution in the experiment and LES, the Schlieren image from experimental case [53,55] (upper half) and the gradient of the calculated density in LES (lower half) are shown in Fig. 2b. The green line in the LES shows the isocontour of $Z = 0.001$. The yellow line illustrates the reported mean cone angle (21.5°) in the experimental measurements [74].

4.1.2. Lift-off length and IDT

Figure 3 shows snapshots of the mass fraction of formaldehyde (CH_2O), hydroxyl (OH) radicals and oxygen molecule (O_2) at 1 ms after the start of the first injection, for the single-injection and the P_3D_5 cases. In the figure, the experimentally measured position of lift-off length (LOL), for the single-injection case, is indicated using a horizontal line. This can be compared to the first axial location of the isocontour of $Y_{\text{OH}} = 1.6 \times 10^{-5}$. This value is equal to 2% of the quasi-steady maximum value of Y_{OH} in the domain. As can be seen, the axial location of the lifted flame is being predicted well for the single-injection case. The LOL for P_3D_5 at this time has not reached its quasi-steady location yet, since it involves a dwell time of 0.5 ms.

By comparing single- and pre-injection cases, it can be seen that the OH concentration for the single-injection case is the highest near the stoichiometric line, where the O_2 concentration is low. However, in the P_3D_5 case, a widespread region with a high level of OH is seen in the fuel-lean mixture downstream, where a significant amount of O_2 is left. These results show that the single-injection case exhibits a classical non-premixed flame, whereas in P_3D_5 due to the injection splitting, a more premixed combustion mode is observed. We will further examine the effects of injection strategies on the combustion mode and emissions in Sections 4.2 to 4.4.

To perform a more quantitative validation on the prediction of spray flame, the instantaneous LOL is plotted in Fig. 4. The LOL is calculated as the first axial location of OH mass fraction reaching 2% of its maximum in the domain (ECN recommendation [53]). As can be seen, shortly after the onset of ignition (≈ 0.4 ms), the flame propagates quickly toward the injector and reaches its quasi-steady location. It subsequently starts to oscillate between, approximately 16 mm and 18 mm, in both experiment and LES. The time-averaged values in the interval of 0.5 ms to 1.7 ms are also denoted by the dashed line and the dotted-dashed line for the experiment (16.66 mm) and the LES (16.93 mm), respectively.

The IDT in LES is defined as the time when the maximum $dT_{\text{max}}(t)/dt$ occurs (ECN recommendation [53]). Fig. 5 shows the temporal evolution of the maximum temperature in the domain $T_{\text{max}}(t)$ (black line) and its derivative, $dT_{\text{max}}(t)/dt$ (red line). The first and second stages of ignition are captured in the simulation and are exhibited by the first and second peaks of $dT_{\text{max}}(t)/dt$.

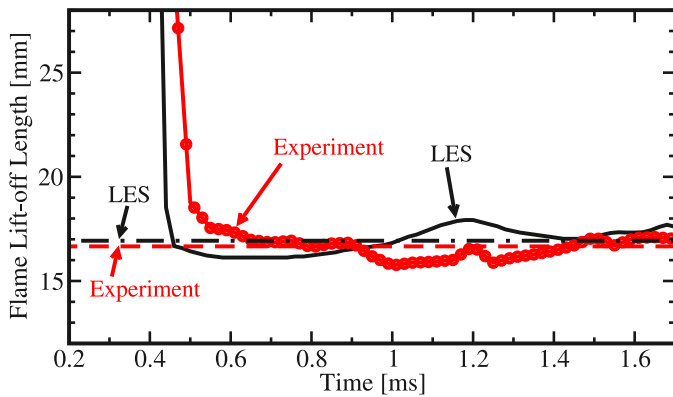


Fig. 4. Temporal evolution of LOL for the single-injection case. The dashed and dashed-dotted lines are the time-averaged values in the interval of 0.5 ms to 1.7 ms.

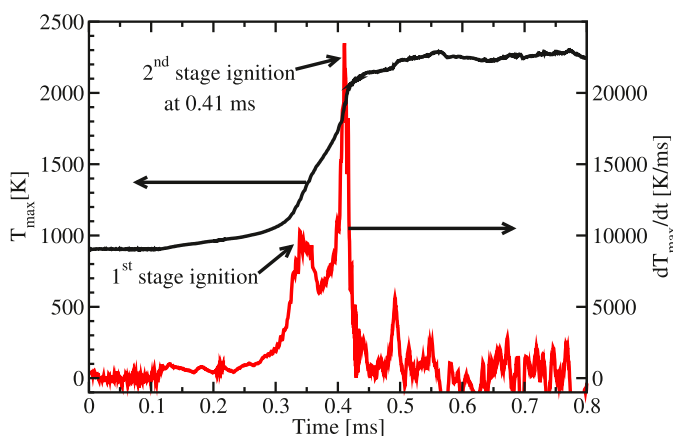


Fig. 5. Temporal evolution of LES calculated maximum temperature $T_{max}(t)$ (black line and left axis) and its time derivative $dT_{max}(t)/dt$ (red line and right axis) for the single-injection case.

The calculated IDT in the single-injection case using this method is 0.41 ms and the measured IDT in the experiment is 0.43 ms [54].

For the double-injection case (P_3D_5), the IDT of the pre-injection fuel using the described method is 0.37 ms, which is slightly shorter than the IDT of a single-injection. This is probably because the pre-injection ends at 0.3 ms and the entrained air during the dwell time improves fuel/air mixing. Therefore, it ignites slightly faster than a single-injection.

The IDT for the second-injection fuel cannot be defined using $dT_{max}(t)/dt$, as it is for the first injection, because $T_{max}(t)$ reaches its maximum after combustion of the pre-injection. Therefore, the IDT for the second injection, in both the experiment and LES, is approximated using the apparent heat release rate (AHRR) as it is recommended in Ref. [8]. The estimated IDT using the LES is 0.22 ms, which is comparable to the experimental estimated value of 0.16 ± 0.02 ms [2].

As mentioned before, to examine the sensitivity of the results to the number of stochastic fields, in addition to the baseline simulation with $N_{SF} = 8$, two additional simulations with different N_{SF} are performed for the single-injection case. The calculated IDT in cases with $N_{SF} = 4, 8, 16$ are 0.43 ms, 0.41 ms and 0.42 ms, respectively. The calculated LOL for these cases are 17.5 mm, 16.9 mm and 17.6 mm, respectively. These values show an insignificant sensitivity to the N_{SF} , which is in line with the literature that suggests sufficiency of 8 stochastic fields [44]. A complete N_{SF} -independence may need a higher number of stochastic fields but by considering the computational costs, $N_{SF} = 8$ is considered to be a reason-

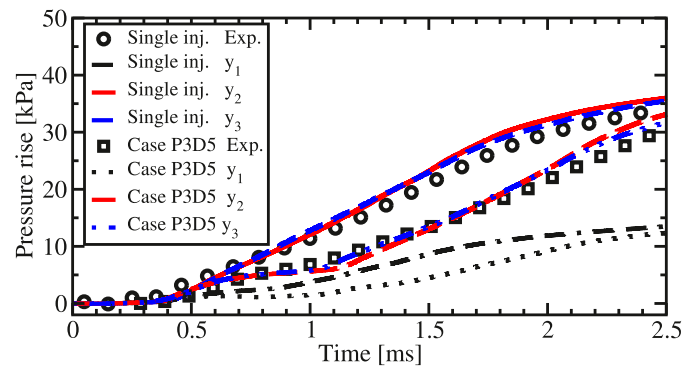


Fig. 6. LES predicted and measured [2,54] pressure rise for single-injection and P_3D_5 cases.

able choice, which yields a balance between accuracy and computational efficiency.

4.1.3. Pressure rise

The predicted pressure rise for both the single-injection and the P_3D_5 cases are shown in Fig. 6.

It can be seen that the LES result with the baseline RPV, y_2 , is almost identical with that of the optimized RPV, y_3 , for both single- and double-injection cases, where both the results with y_2 and y_3 agree well with the experiments. However, the commonly used RPV, y_1 , yields a poor prediction of the pressure rise. Unlike y_2 and y_3 , y_1 does not increase monotonically after the ignition [26]. Therefore, it does not represent the entire progress in the ignition reactions.

4.1.4. Temporal-spatial structure of flame and soot

The LES model performance in the prediction of the detailed structure of the spray flame is examined in Fig. 7. The top row in this figure shows the combustion chemiluminescence and the soot luminosity from the experiment for the single-injection case [53,75]. The high-temperature reactivity border is also indicated using the blue line. The middle row shows the simulation results of the line-of-sight distribution of formaldehyde (blue) and OH (yellow), as well as an isocontour of $T = 1100$ K (white line). The bottom row shows the LES results of the line-of-sight distribution of soot (black), as well as the same isocontours of $T = 1100$ K (blue line). In the LES results, the first ignition site can be seen at 0.4 ms, at the alike time and axial and radial location as it was observed in the experiment. Following the onset of ignition, the high-temperature region develops both radially and axially, similar to that in the experiment.

To the best of the authors' knowledge, the evolution of the soot mass has not been reported in the experimental measurements for any of the studied cases, which have rather short injection durations. Therefore, to adopt the surface growth coefficient (see Ref. [49]) and to examine quantitatively the performance of the model in trend prediction of soot mass evolution, the available reported soot mass for the case from Refs. [53,76] is used. This case has a similar injection rate and thermodynamic conditions but a longer injection (6 ms) than the current case (1.5 ms). As can be seen in Fig. 8, although the onset of soot formation is predicted to be slightly (≈ 0.2 ms) earlier than that in the experiment, the trend of this evolution is fairly well predicted. This can be understood by comparing the LES results with the measurement before 1.5 ms.

In the following sections, we use the current validated LES model to study the effects of pre-injection on the ignition, combustion and emissions of the main-injection.

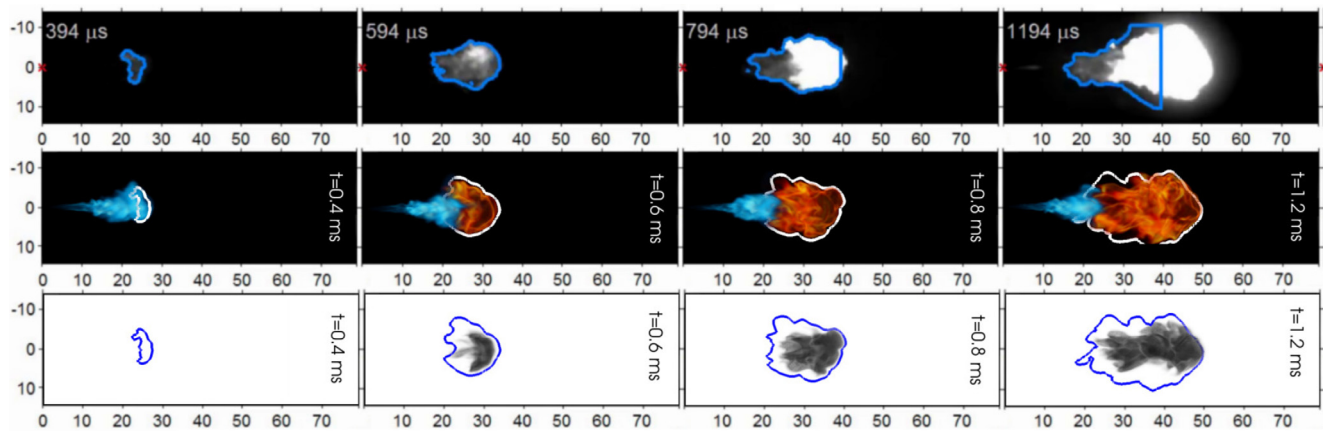


Fig. 7. Top row: the combustion chemiluminescence and the soot luminosity from the experiment [53,75]. Middle row: the simulation results of line-of-sight distribution of formaldehyde (blue) and OH (yellow). Bottom row: the simulation results of the line-of-sight distribution of soot (black). The lines are isocontour of “high-temperature reactivity border” from the experiment [53,75] and isocontour of $T = 1100$ K from the simulation.

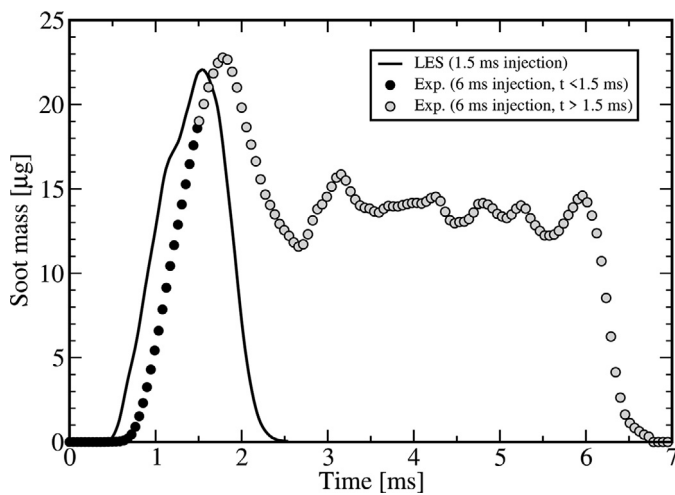


Fig. 8. Calculated mass of soot in the current LES (1.5 ms injection) compared with mass of soot for an alike experimental case with longer injection (6 ms) [53,76]. The mass of soot for the original experiment with 1.5 ms injection has not been reported.

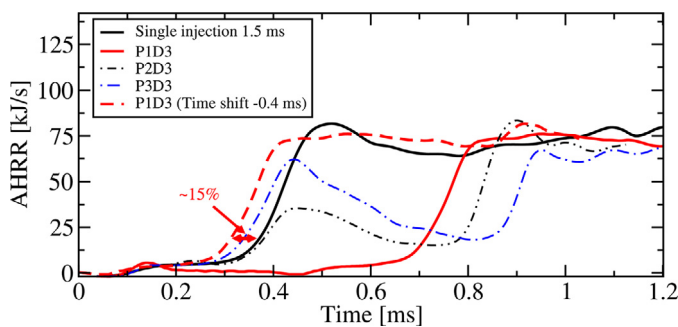


Fig. 9. The apparent heat release rate for cases with different duration and mass of pre-injection. The P_1D_3 (red line) is advanced by 0.4 ms and is represented by red dashed-line in order to be comparable with the single-injection case.

4.2. Effects of pre-injection on the ignition of the main-injection

Fig. 9 shows the AHRR for the single-injection case and the three double-injection cases with the same dwell time of 0.3 ms (i.e., P_1D_3 , P_2D_3 and P_3D_3). It can be seen that the AHRR for cases P_2D_3 (with 0.2 ms pre-injection) and P_3D_3 (with 0.3 ms pre-injection) have peaks of AHRR in the vicinity of 0.44 ms, which

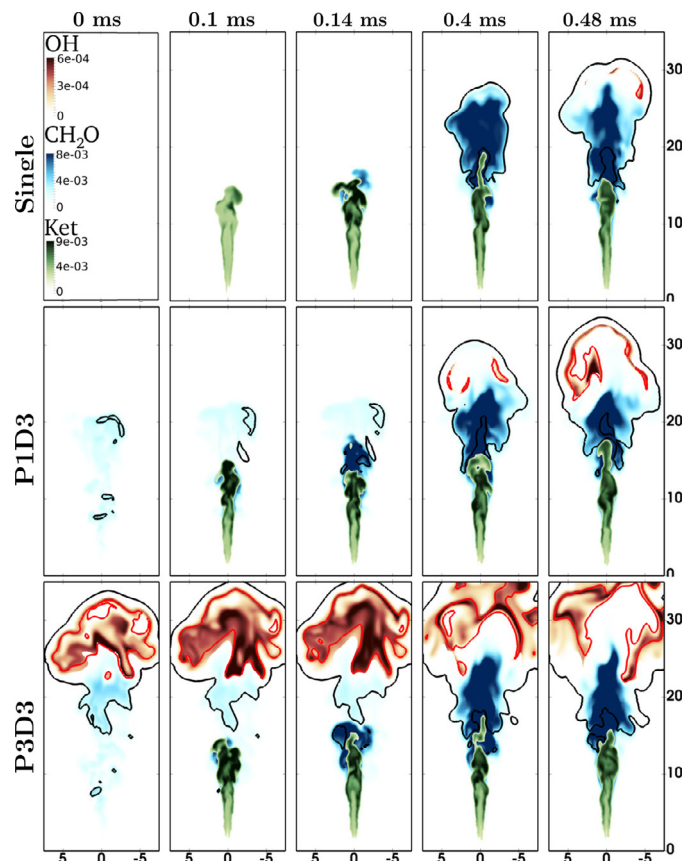


Fig. 10. The snapshots of KET, CH_2O and OH radicals for the single-injection, P_1D_3 and P_3D_3 cases. The shown values of times are t_{AMI} . To simultaneously illustrate the distribution of low- and high-temperature areas, isocontour of $T = 950$ K (black line) and $T = 2000$ K (red line) are also shown.

are well before the start of the main-injection. It implies that in these cases the pre-injection ignites and releases heat before the start of the main-injection. However, the P_1D_3 case, which has the shortest pre-injection duration (0.1 ms), has essentially no significant AHRR until around 0.7 ms, which is 0.3 ms after the start of the main-injection. This is because such a short pre-injection is quickly diluted by the ambient air entrainment during the dwell time, and fails to auto-ignite. Despite its failure in igniting, the pre-injection is shown to decrease the IDT of the main-injection by 15%

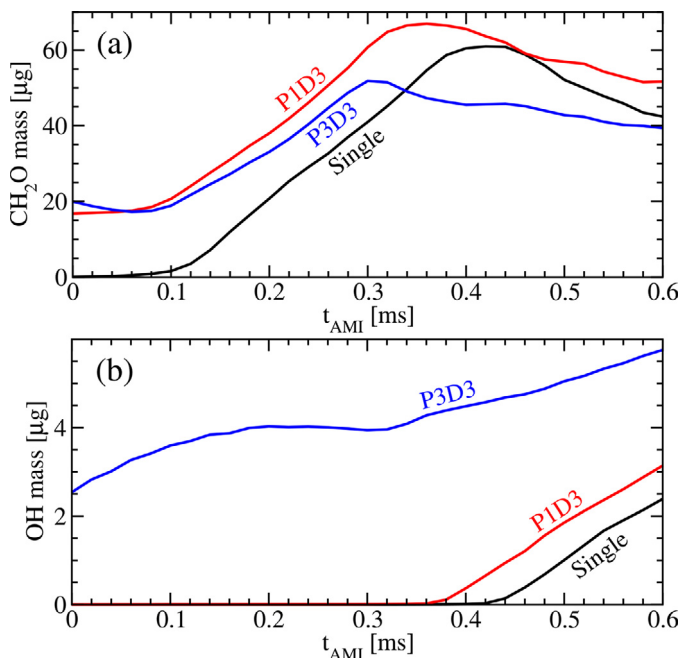


Fig. 11. Temporal evolution of total mass of (a) CH₂O; (b) OH; in the domain after start of the main injection for the same cases as in Fig. 10.

as compared to that of the single-injection case. This is confirmed by advancing the results for this case by 0.4 ms, which is the start time of the main-injection in this case. A similar decrease of the main-injection IDT in the cases P₂D₃ and P₃D₃ are observed. However, the underlying physical mechanism for the reduction of IDT in these two cases (with a longer pre-injection) is different from that for the P₁D₃ case. The underlying mechanisms are discussed in the following, based on the LES results.

Fig. 10 shows distribution of ketohydroperoxide (KET), CH₂O and OH radicals for the single-injection case, P₁D₃ case (representing shorter pre-injection) and P₃D₃ case (representing longer pre-injection). The selected times for illustration are after the start of the main-injections for all three cases. Hereinafter, we refer to “the time after the start of the main-injection” as t_{AMI} , i.e., for single-injection case $t_{AMI} = t$; for case P₁D₃ $t_{AMI} = t - 0.4$ ms; and for P₃D₃ $t_{AMI} = t - 0.6$ ms, where t is the time after start of the first injection event. The sequences of snapshots in the same t_{AMI} in this figure are used to demonstrate how the ignition and the cool flame are different in the main-injection in these three cases. The ignition and high-temperature flame are indicated by OH distribution and red isocontours of $T = 2000$ K, while the cool flame is indicated by KET and CH₂O distributions as well as the black isocontour of $T = 950$ K.

As mentioned before, the fuel delivered during the pre-injection in P₁D₃ is quickly diluted by the ambient air during the dwell time and fails to auto-ignite. This can be seen in the snapshots of this case between 0 - 0.14 ms, where neither OH radicals nor high-temperature regions have formed. The existence of the radicals from the pre-injection mixture in this case, however, promotes the formation of CH₂O, KET and other cool flame products. These species also elevate the local temperature by about 50 K, compared to those in the single-injection case. This cool flame boosts the onset of high-temperature ignition of the main-injection. Therefore, at $t_{AMI} = 0.4$ ms the first ignition site can be seen for P₁D₃ case, while there is no such a significant ignition site for the single-injection case at the same time instance.

To support this discussion quantitatively, the mass evolutions of CH₂O and OH for the same cases as in Fig. 10 are shown in Fig. 11.

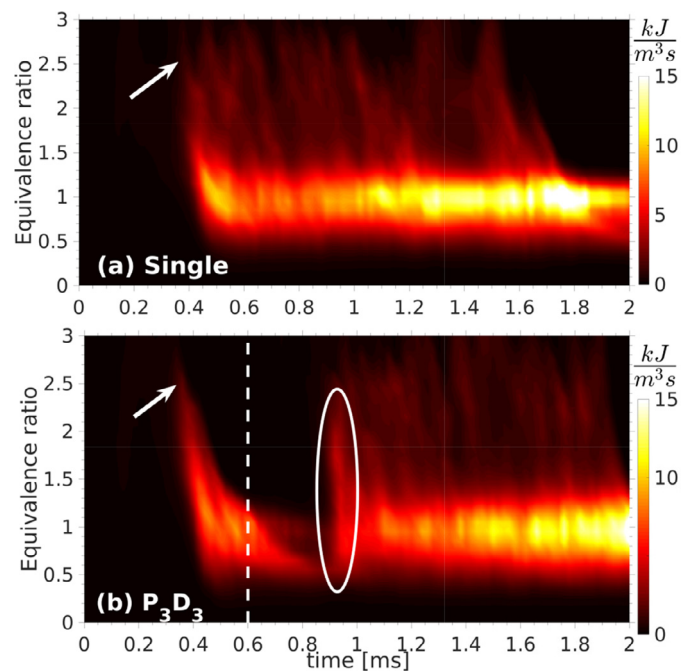


Fig. 12. Temporal evolution of the sum of heat release rate conditional on given equivalence ratios in the entire LES domain for the (a) single-injection and (b) P₃D₃ cases.

As can be seen in the latter figure at the start of main-injection in P₁D₃, while a considerable amount of CH₂O exists in the domain, no OH has been formed yet. As discussed, this cool flame product, however, advances the formation of OH which can be confirmed by comparing OH mass of P₁D₃ and single-injection cases in Fig. 11b.

Unlike the P₁D₃ case, in P₃D₃ case, a high-temperature zone and OH radicals have been established in the domain before the start of the main-injection (see for instance $t_{AMI} = 0$ ms in Figs. 10 and 11 b). The fuel delivered during the main-injection event penetrates into this high-temperature zone formed after pre-injection and immediately ignites. We will further examine the ignition and combustion mode of the cases with a 0.3 ms pre-injection, in the following section.

4.3. The combustion mode of pre- and main-injections

As mentioned in Section 2.4, the concept of flamelet generated manifold is to apply a manifold of flamelets that consists of non-premixed combustion (steady flamelets) and local ignition/combustion of a premixed mixture (unsteady flamelets) [77]. This low-dimensional manifold is constructed based on a progress variable which allows modeling the local ignition and combustion process in the premixed mixture.

Fig. 12 shows the temporal evolution of the total heat release rate in the domain for given ϕ values (the vertical axis). Integration of the total heat release rate in the ϕ coordinate gives the total heat release rate of the entire mixture in the domain. For the single-injection case, there is no significant heat release until 0.4 ms. The first ignition site is in the fuel-rich mixture, with $\phi \approx 2.5$ (see the white arrow). Shortly after the onset of ignition, the heat release shifts toward stoichiometric and fuel-lean mixtures. During the time interval of 0.4 ms (onset of ignition) and 1.5 ms (end of injection), the heat release rate distribution in the ϕ -coordinate is rather similar and has a maximal around the stoichiometric mixtures, $\phi = 1$. This indicates a quasi-steady lifted diesel spray flame. Analysis of the flame index indicates that the

later stage combustion is mainly in the diffusion flame mode for the single-injection case (will be shown later). The structure of the quasi-steady lifted flame at $t = 1$ ms can be found in Fig. 3.

For the double-injection case, although the ignition start of pre-injection occurs in the fuel-rich mixture, which is akin to the single-injection case, it does not develop into a lifted diffusion flame. This is attributed to the short duration of the pre-injection, ending before the onset of high-temperature ignition. The fuel/air mixture from the pre-injection is burned mainly in the premixed combustion mode, exhibiting a heat release rate shifting toward $\phi = 0.5 - 1$. For this reason, as it will be shown in Section 4.4, soot formation during the pre-injection is low, which is in line with the observation in Ref. [2].

The white dashed line in Fig. 12b illustrates the start of the main-injection at 0.6 ms. At approximately 0.9 ms, the fuel delivered in the main-injection starts to release heat which can be seen in this figure and also in Fig. 9. However, the onset of heat release in the main-injection is different from that in the first injection. Here, instead of having a rich-zone ignition like the single- and pre-injection (highlighted by white arrows), the heat release appears within a wide equivalence ratio range of $0.5 < \phi < 2$ (highlighted by a white oval). When the main-injection mixture enters into the high-temperature zone of the burned gas from the pre-injection, it is ignited immediately. Therefore, the heat starts to be released in a wide range of equivalence ratios, rather than having slow auto-ignition in a limited number of ignition sites. The ignition of the main-injection in P_3D_3 can also be seen in form of an OH rise in Fig. 11 at $t_{AMI} \approx 0.3$ ms (i.e., $t \approx 0.9$ ms in Fig. 12).

To complete the presented image of combustion of pre- and main-injection, the mode of combustion is investigated using flame index (FI) in a similar approach that was practised in Ref. [78]. FI can be defined by the degree of alignment of fuel and oxidizer gradients as

$$FI = \frac{\nabla Y_F \cdot \nabla Y_{O_2}}{|\nabla Y_F| |\nabla Y_{O_2}|}, \quad (8)$$

where Y_F is mass fraction of fuel ($C_{12}H_{26}$) and all smaller C_xH_y species. Two regions are defined using the local distribution of FI : (1) the local region with negative FI values as gradients-opposed or non-premixed combustion region; (2) the local region with positive FI values as gradients-aligned or premixed combustion region. $HRR_{non-premixed}$ and $HRR_{premixed}$ is defined as the fraction of the heat release rate (HRR) from each of the corresponding regions. To investigate the effect of splitting the single-injection to a pre- and main-injections on the combustion mode, the $HRR_{premixed}$ of cases single-injection, P_3D_3 and P_3D_5 are plotted in Fig. 13. As can be seen, the pre-mixed combustion level is higher in the multiple-injection cases than that in single-injection case. The more intense premixed combustion is being observed during and shortly after the dwell times between the two injections. The dwell times are from 0.3 ms to 0.6 ms in P_3D_3 and from 0.3 ms to 0.8 ms in P_3D_5 .

4.4. Effects of pre-injection duration and dwell time on the soot formation/oxidation of the main-injection

It has been reported in the experiments [79] that a shorter dwell time in double injection cases leads to a lower soot emission. To investigate the experimental observation in the reduction of net soot, we plot the temporal evolution of the total soot mass for the single-injection and the double-injection P_3D_3 and P_3D_5 cases in Fig. 14. The latter two cases have similar durations of first and second injections, but different dwell times. As can be seen, the P_3D_5 case exhibits a higher peak soot mass than that in the single-injection case, while in the P_3D_3 case the peak soot mass appears to be lower. The underlying physical reason for this result will be discussed in the following.

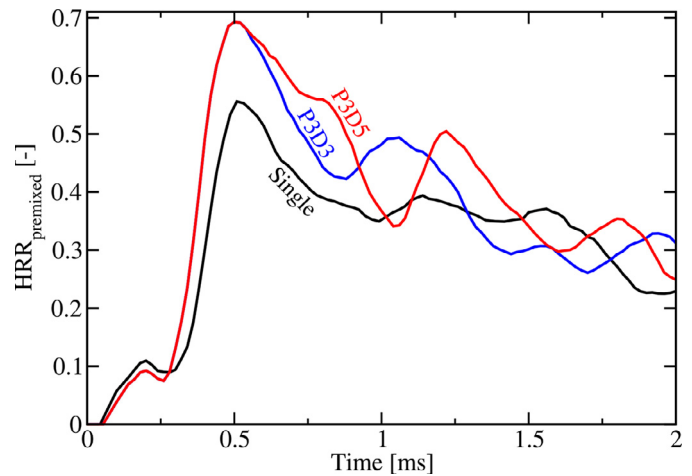


Fig. 13. The fraction of premixed heat release rate for single- and pre-injection cases. See the text for the definition of $HRR_{premixed}$.

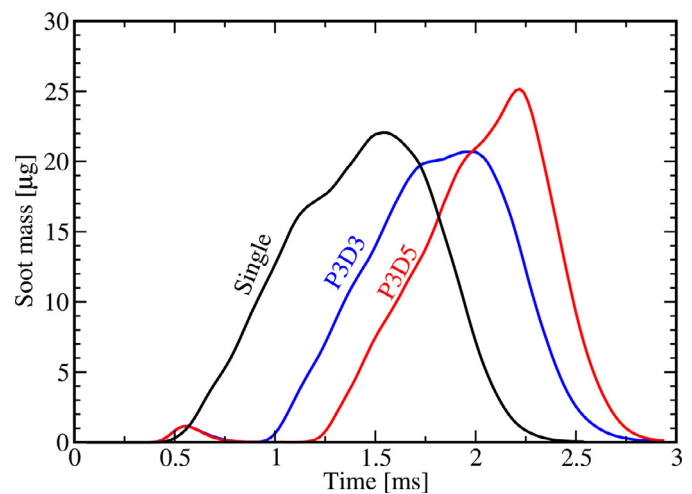


Fig. 14. Evolution of soot mass for single- and pre-injection cases with long and short dwell times.

Fig. 15 shows the distribution of soot formation/oxidation rates (dM_{soot}/dt), for different cases at five instances of time after the start of the main-injection. It is observed in the LES results that a major fraction of net soot formation ($dM_{soot}/dt > 0$) takes place in the region with $1500 \text{ K} < T < 2000 \text{ K}$ (hereinafter is referred to as the intermediate-temperature region) and $\phi > 1.5$. The major fraction of soot oxidation ($dM_{soot}/dt < 0$) takes place in the region with $T > 2000 \text{ K}$ (hereinafter is referred to as the high-temperature region). To illustrate the overlap of these intermediate- and high-temperature regions with the soot formation and oxidation regions, respectively, the isocontours of $T = 1500 \text{ K}$ (red) and $T = 2000 \text{ K}$ (green) are plotted in Fig. 15. These regions are used to investigate the effects of pre-injection timings on modifying the local temperature and, hence, local soot formation/oxidation. The distribution of temperature at the same time instances is also shown in Fig. 16. Isocontour of $\phi = 1.5$, indicating the fuel-rich zone, is shown in both figures with black lines.

As can be seen, the soot formation and oxidation rates at $t_{AMI} = 0.4$ ms are higher in the P_1D_3 case than that in the single-injection case. A comparison between the isocontour of ϕ in these two cases shows that the fuel-rich areas in both cases are almost the same. However, both intermediate- and high-temperature regions for the case with pre-injection (P_1D_3) are broader. This is

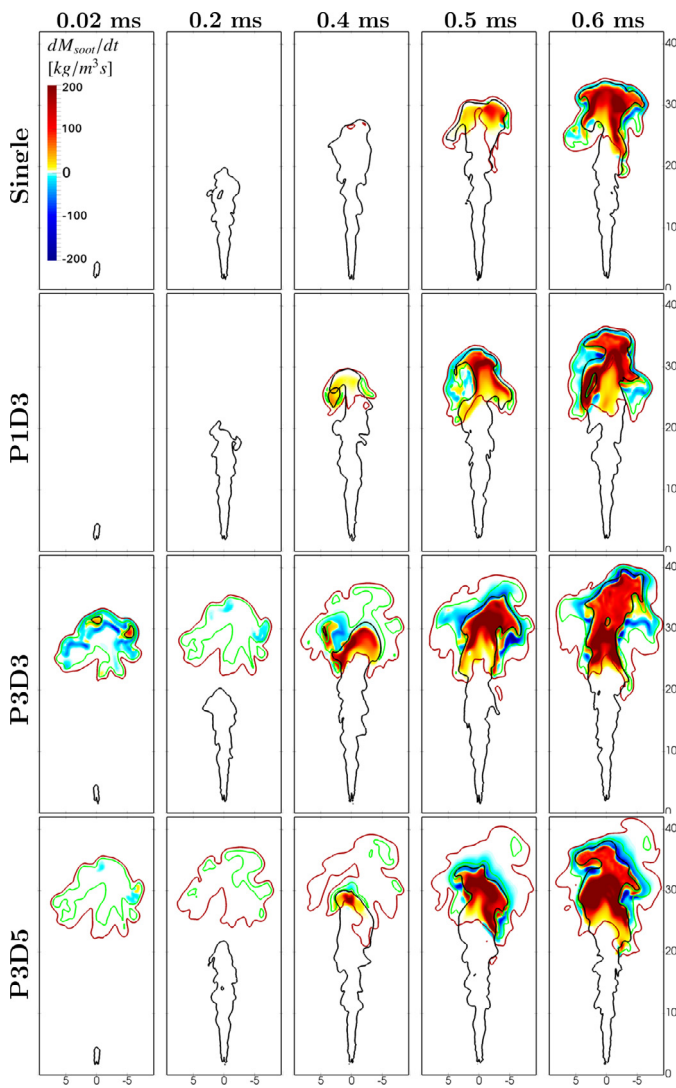


Fig. 15. Distribution of soot formation/oxidation rates. The shown times are t_{AMI} . The yellow color shows the rate of formation; the blue color shows the rate of oxidation (see the color bar); the red line is isocontour of $T = 1500$ K; the green line is isocontour of $T = 2000$ K; the black line is isocontour of $\phi = 1.5$.

due to the earlier ignition of the main-injection in P_1D_3 than that in the single-injection case, as discussed in Section 4.2.

By increasing the pre-injection fuel amount in the case P_3D_3 , the formation and oxidation of soot are further elevated. Unlike case P_1D_3 which has a short non-igniting pre-injection, the main-injection in the P_3D_3 case directly penetrates into the intermediate- and high-temperature plumes formed after the pre-injection due to the relatively short dwell time. This penetration of the main-injection into intermediate- and high-temperature plumes gives rise to the higher soot formation and oxidation.

For case P_3D_5 , the dwell time is longer, which in turn, provides a longer time for the fresh air entrainment to cool down the pre-injection mixture before penetration of main-injection. By comparing the temperature distribution of pre-injection in cases P_3D_3 and P_3D_5 in Fig. 16 during $t_{AMI} = 0.02$ ms - 0.4 ms, it can be seen that the high-temperature region which is important for soot oxidation has been decreased in P_3D_5 . This is illustrated quantitatively in Figs. 17a and b by showing the total mass of the intermediate- and high-temperature regions, respectively, after the start of the main-injections. As discussed, P_3D_3 exhibits a larger high-temperature region and a smaller intermediate-temperature region compared to those in P_3D_5 . This condition in P_3D_3 is in favor of more soot

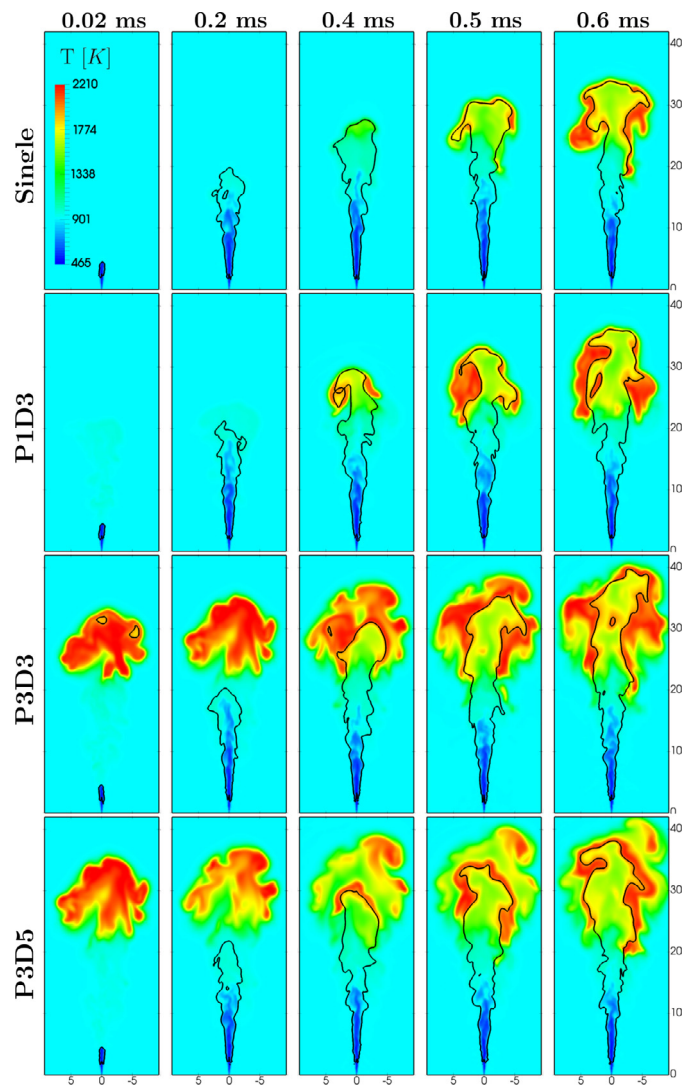


Fig. 16. Distribution of temperature at the same time instances as Fig. 15. The shown times are t_{AMI} . The black line is isocontour of $\phi = 1.5$.

oxidation compared to the other case. This can be confirmed by comparing the soot formation/oxidation results for P_3D_3 and P_3D_5 during 0.2 ms - 0.5 ms in Fig. 15. In this figure, the rate of local soot oxidation in P_3D_3 is higher than that in P_3D_5 . Therefore, as it was observed in Fig. 14, for the P_3D_3 , which provides a larger high-temperature region compared to P_3D_5 , the peak soot mass appears to be lower.

5. Conclusion

A hybrid T-PDF/FGM model for LES modeling of spray combustion is presented, validated and used to study the effects of duration of pre-injection and dwell time on the combustion of spray in diesel engine-like conditions. The main findings of this study are summarized as follows.

(1) The fuel from the pre-injection can be fully oxidized generating a high-temperature region prior to the main-injection when the pre-injection is sufficiently long. Fuel from a too-short pre-injection can still promote the ignition of the main-injection, attributed to the cool flame formed in the pre-injection mixture, without releasing any significant amount of heat prior to the start of the main-injection.

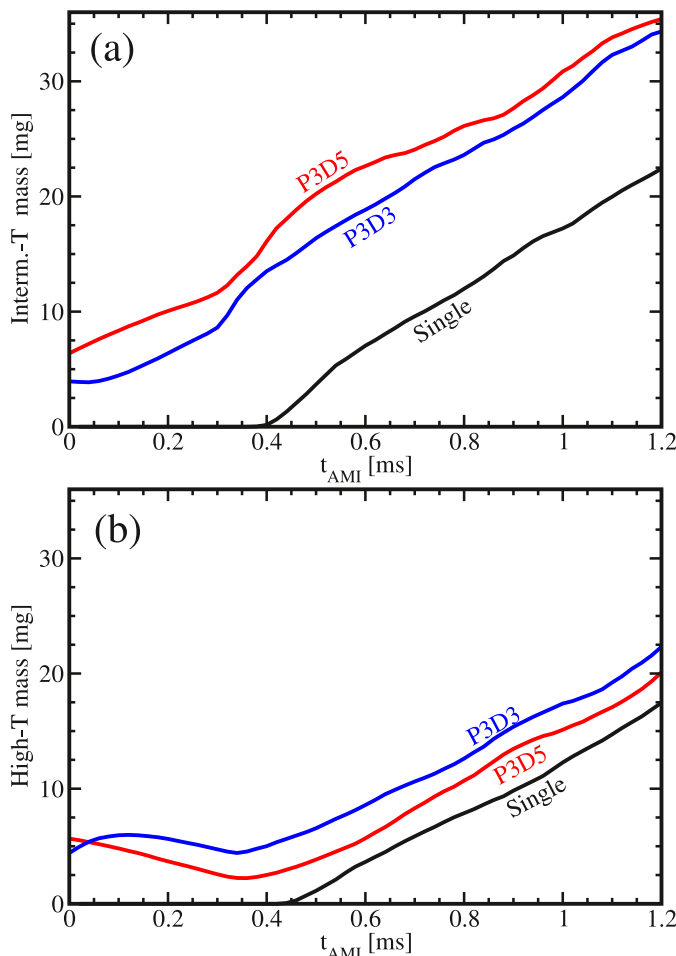


Fig. 17. Evolution of mass of the mixture in (a) intermediate- and (b) high-temperature regions (see the text for the definitions of these regions) after the start of the main-injection.

(2) Splitting the single-injection into pre- and main-injections shifts the combustion mode toward lean and premixed combustion during and slightly after the dwell time. The effect is suppressed shortly after the start of the main-injection.

(3) Three mechanisms for the soot emission in the pre-injection strategy are postulated. (a) For small pre-injection, the cool flame products and heat release of the pre-injection enhance the ignition of the main-injection, which in turn enhances both formation and oxidation of soot. (b) For the cases with sufficiently long pre-injection and moderate dwell time, the fuel penetration of the main-injection into the intermediate- and high-temperature combustion products of the pre-injection can substantially increase the soot formation and oxidation by enriching the reactants. (c) If the dwell time is long, it can provide extra entrainment of fresh air into the high-temperature region of the pre-injection. Therefore, the combustion product of the pre-injection is cooled down to intermediate temperatures, which slows down the soot oxidation.

(4) Within the pre-injection and dwell time ranges that are examined here, it is found that decreasing dwell time can reduce the peak soot mass in the domain, due to the larger high-temperature region and thus the enhanced soot oxidation.

Declaration of Competing Interest

The authors declare that they have no known competing financial interests or personal relationships that could have appeared to influence the work reported in this paper.

Acknowledgments

This work was sponsored by the Swedish Research Council (VR) and the Swedish Energy Agency through KC-CECOST. The computation was performed using the computer facilities provided by the Swedish National Infrastructures for Computing (SNIC).

Appendix A. Resolved fraction of the turbulence

To examine the sufficiency of the grid and filter size in resolving the turbulent kinetic energy (TKE), we have performed 10 realizations of the non-reacting LES case. Different realizations are generated by randomly changing the temporal order of the injected droplets diameter, while the overall Rosin Rammler distribution of the droplets are kept identical. Using these 10 LES realization, the ensemble-averaged velocity and its fluctuation can be calculated. Then the resolved scale turbulent kinetic energy, k_{res} (Eq. 9) can be estimated and used to assess the quality of the current LES.

$$k_{res}(x, y, z, t) = \frac{1}{2}((u'_i)^2 + (u'_j)^2 + (u'_k)^2) \quad (9)$$

where $u'_i = u_i - \langle u_i \rangle$ is the fluctuation of axial velocity, and u'_j and u'_k are the corresponding ones of the other two velocity components. $\langle \rangle$ denotes ensemble average with the 10 LES runs. The total turbulence kinetic energy (k) consists of the resolved (k_{res}) and the subgrid-scale turbulent kinetic energy (k_{sgs})

$$\langle k(x, y, z, t) \rangle = \langle k_{res}(x, y, z, t) \rangle + \langle k_{sgs}(x, y, z, t) \rangle. \quad (10)$$

Figs. 18 a and b show the $\langle k_{sgs} \rangle$ and $\langle k_{res} \rangle$, respectively, at $t = 1$ ms, for the studied case which has a nozzle diameter of 90 μm . Comparing these two fields indicates the fraction of resolved turbulence in the current LES. To quantitatively perform such comparison, the fraction of resolved turbulent kinetic energy (i.e., $\langle k_{res} \rangle / (\langle k_{res} \rangle + \langle k_{sgs} \rangle)$) is shown in Fig. 19 for various downstream locations. These axial locations are indicated by white lines in Fig. 18. As can be seen, except for a limited zone near the centerline, an acceptable fraction of turbulence kinetic energy is resolved. It should be noted that in the Lagrangian particle tracking approach, the in-nozzle and breakup processes are not resolved

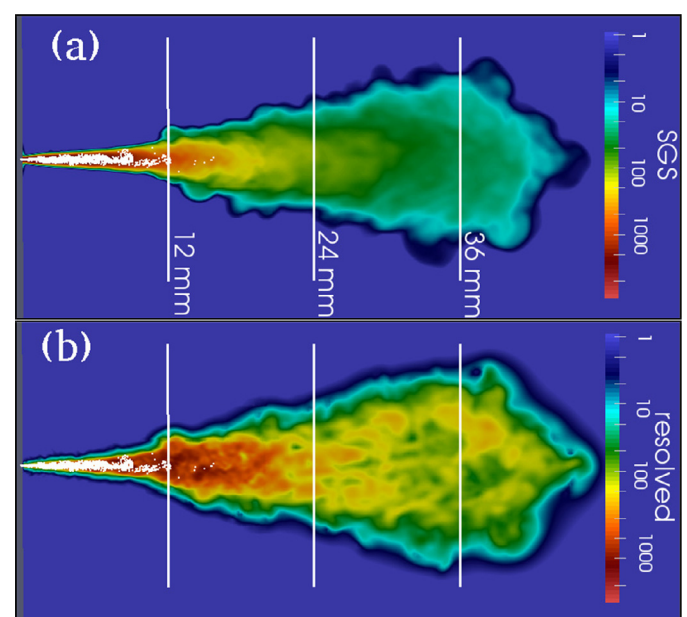


Fig. 18. (a) $\langle k_{sgs} \rangle$; (b) $\langle k_{res} \rangle$ at $t = 1$ ms. The white lines show the axial locations of the plots in Fig. 19.

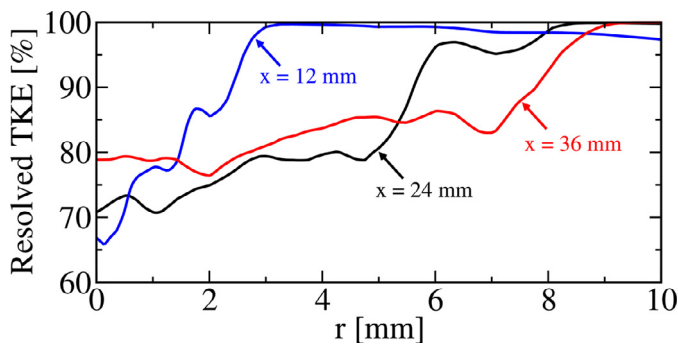


Fig. 19. The fraction of resolved turbulent kinetic energy $\langle k_{res} \rangle / (\langle k_{res} \rangle + \langle k_{sgs} \rangle)$ at three axial locations.

within CFD cell resolutions but are modeled via the so-called primary and the secondary atomization sub-models. It should also be noted that the majority of combustion is expected to take place in relatively large axial locations as the measured flame lift-off length is 16.5 mm [53]. Thus, it is judged that the present LES grid and filter size are sufficiently fine to resolve the turbulent kinetic energy for the purpose of this study.

References

- [1] M.J. Borz, Y. Kim, J. O'Connor, The effects of injection timing and duration on jet penetration and mixing in multiple-injection schedules, Technical Report, SAE Technical Paper, 2016.
- [2] A.A. Moiz, M.M. Ameen, S.-Y. Lee, S. Som, Study of soot production for double injections of n-dodecane in ci engine-like conditions, *Combust. Flame* 173 (2016) 123–131.
- [3] M. Bolla, M.A. Chishty, E.R. Hawkes, S. Kook, Modeling combustion under engine combustion network spray a conditions with multiple injections using the transported probability density function method, *Int. J. Engine Res.* 18 (1–2) (2017) 6–14.
- [4] N. Maes, P. Bakker, N. Dam, B. Somers, Transient flame development in a constant-volume vessel using a split-scheme injection strategy, *SAE Int. J. Fuels Lubr.* 10 (2) (2017) 318–327.
- [5] S.K. Chen, Simultaneous reduction of nox and particulate emissions by using multiple injections in a small diesel engine, *SAE Int. J. Engines* (2000) 2127–2136.
- [6] T. Tow, D. Pierpont, R.D. Reitz, Reducing particulate and no x emissions by using multiple injections in a heavy duty di diesel engine, *SAE Int. J. Engines* (1994) 1403–1417.
- [7] J. O'Connor, M. Musculus, Post injections for soot reduction in diesel engines: a review of current understanding, *SAE Int. J. Engines* 6 (1) (2013) 400–421.
- [8] S. Skeen, J. Manin, L.M. Pickett, Visualization of ignition processes in high-pressure sprays with multiple injections of n-dodecane, *SAE Int. J. Engines* 8 (2015) 696–715.
- [9] Q. Zhou, T. Lucchini, G. D'Errico, N. Maes, B. Somers, X.-c. Lu, Computational modeling of diesel spray combustion with multiple injections, Technical Report, SAE Technical Paper, 2020.
- [10] W. Zhao, H. Wei, M. Jia, Z. Lu, K.H. Luo, R. Chen, L. Zhou, Flame-spray interaction and combustion features in split-injection spray flames under diesel engine-like conditions, *Combust. Flame* 210 (2019) 204–221.
- [11] A. Hadadpour, M. Jangi, K.M. Pang, X.S. Bai, The role of a split injection strategy in the mixture formation and combustion of diesel spray: a large-eddy simulation, *Proc. Combust. Inst.* 37 (2019) 4709–4716.
- [12] J. Cao, X. Leng, Z. He, Q. Wang, W. Shang, B. Li, Experimental study of the diesel spray combustion and soot characteristics for different double-injection strategies in a constant volume combustion chamber, *J. Energy Inst.* 93 (1) (2020) 335–350.
- [13] K. Yang, H. Yamakawa, K. Nishida, Y. Ogata, Characteristics of free spray development, mixture formation, and combustion under high-pressure split injection, *Atomization Sprays* 28 (3) (2018) 217–240.
- [14] A. Hadadpour, M. Jangi, X.S. Bai, The effect of splitting timing on mixing in a jet with double injections, *Flow, TurbulenceCombust.* 101 (4) (2018) 1157–1171.
- [15] H.G. How, H.H. Masjuki, M. Kalam, Y.H. Teoh, Influence of injection timing and split injection strategies on performance, emissions, and combustion characteristics of diesel engine fueled with biodiesel blended fuels, *Fuel* 213 (2018) 106–114.
- [16] J. Liu, H. Wang, Z. Zheng, L. Li, B. Mao, M. Xia, M. Yao, Improvement of high load performance in gasoline compression ignition engine with pde and multiple-injection strategy, *Fuel* 234 (2018) 1459–1468.
- [17] A. Hadadpour, M. Jangi, X.S. Bai, Jet-jet interaction in multiple injections: alarge-eddy simulation study, *Fuel* 234 (2018) 286–295.
- [18] J. O'Connor, M.P. Musculus, L.M. Pickett, Effect of post injections on mixture preparation and unburned hydrocarbon emissions in a heavy-duty diesel engine, *Combust. Flame* 170 (2016) 111–123.
- [19] C.K. Blomberg, L. Zeugin, S.S. Pandurangi, M. Bolla, K. Boulouchos, Y.M. Wright, Modeling split injections of ECN "spray a" using a conditional moment closure combustion model with rans and LES, *SAE Int. J. Engines* 9 (2016-01-2237) (2016) 2107–2119.
- [20] W. Jing, Z. Wu, W.L. Roberts, T. Fang, Spray combustion of biomass-based renewable diesel fuel using multiple injection strategy in a constant volume combustion chamber, *Fuel* 181 (2016) 718–728.
- [21] C. Chartier, O. Andersson, B. Johansson, M. Musculus, M. Bobba, Effects of post-injection strategies on near-injector over-lean mixtures and unburned hydrocarbon emission in a heavy-duty optical diesel engine, *SAE Int. J. Engines* 4 (2011-01-1383) (2011) 1978–1992.
- [22] S. Som, D.E. Longman, Z. Luo, M. Plomer, T. Lu, P.K. Senecal, E. Pomraning, Simulating flame lift-off characteristics of diesel and biodiesel fuels using detailed chemical-kinetic mechanisms and large eddy simulation turbulence model, *J. Energy Resour. Technol.* 134 (3) (2012) 032204.
- [23] C. Gong, M. Jangi, T. Lucchini, G. D'Errico, X.-S. Bai, Large eddy simulation of air entrainment and mixing in reacting and non-reacting diesel sprays, *Flow, TurbulenceCombust.* 93 (3) (2014) 385–404.
- [24] A. Irannejad, A. Banaeizadeh, F. Jaber, Large eddy simulation of turbulent spray combustion, *Combust. Flame* 162 (2) (2015) 431–450.
- [25] Y. Pei, S. Som, E. Pomraning, P.K. Senecal, S.A. Skeen, J. Manin, L.M. Pickett, Large eddy simulation of a reacting spray flame with multiple realizations under compression ignition engine conditions, *Combust. Flame* 162 (12) (2015) 4442–4455.
- [26] A. Wehrfritz, O. Kaario, V. Vuorinen, B. Somers, Large eddy simulation of n-dodecane spray flames using flamelet generated manifolds, *Combust. Flame* 167 (2016) 113–131.
- [27] S. Gallot-Lavallée, W. Jones, Large eddy simulation of spray auto-ignition under egr conditions, *Flow, Turbulence Combust.* 96 (2) (2016) 513–534.
- [28] P. Kundu, M.M. Ameen, S. Som, Importance of turbulence-chemistry interactions at low temperature engine conditions, *Combust. Flame* 183 (2017) 283–298.
- [29] C.-W. Tsang, Y. Wang, C. Wang, A. Shelburn, L. Liang, K. Puduppakkam, A. Modak, C. Naik, E. Meeks, C. Rutland, Evaluation and validation of Large-Eddy-Simulation (LES) for Gas Jet and Sprays, Technical Report, SAE Technical Paper, 2017.
- [30] H. Kahila, A. Wehrfritz, O. Kaario, V. Vuorinen, Large-eddy simulation of dual-fuel ignition: diesel spray injection into a lean methane-air mixture, *Combust. Flame* 199 (2019) 131–151.
- [31] H. Kahila, O. Kaario, Z. Ahmad, M.G. Masouleh, B. Tekgül, M. Larmi, V. Vuorinen, A large-eddy simulation study on the influence of diesel pilot spray quantity on methane-air flame initiation, *Combust. Flame* 206 (2019) 506–521.
- [32] B. Tekgül, H. Kahila, O. Kaario, V. Vuorinen, Large-eddy simulation of dual-fuel spray ignition at different ambient temperatures, *Combust. Flame* 215 (2020) 51–65.
- [33] S. Xu, S. Zhong, K.M. Pang, S. Yu, M. Jangi, X.-s. Bai, Effects of ambient methanol on pollutants formation in dual-fuel spray combustion at varying ambient temperatures: a large-eddy simulation, *Appl. Energy* 279 (2020) 115774.
- [34] Y. Zhang, S. Xu, S. Zhong, X.-S. Bai, H. Wang, M. Yao, Large eddy simulation of spray combustion using flamelet generated manifolds combined with artificial neural networks, *Energy AI* 2 (2020) 100021.
- [35] M. Pucilowski, M. Jangi, H. Fatehi, K.M. Pang, X.-S. Bai, LES Study of diesel flame/wall interaction and mixing mechanisms at different wall distances, *Proc. Combust. Inst.* (2020) 5597–5604.
- [36] S. Xu, K.M. Pang, Y. Li, A. Hadadpour, S. Yu, S. Zhong, M. Jangi, X.-s. Bai, Les/tpdf investigation of the effects of ambient methanol concentration on pilot fuel ignition characteristics and reaction front structures, *Fuel* 287 (2021) 119502.
- [37] S. Zhong, S. Xu, X.-S. Bai, A. Hadadpour, M. Jangi, F. Zhang, Q. Du, Z. Peng, Combustion characteristics of n-heptane spray combustion in a low temperature reform gas/air environment, *Fuel* 293 (2021) 120377.
- [38] M. Zhang, J.C. Ong, K.M. Pang, X.-S. Bai, J.H. Walther, An investigation on early evolution of soot in n-dodecane spray combustion using large eddy simulation, *Fuel* 293 (2021) 120072.
- [39] J.C. Ong, K.M. Pang, J.H. Walther, Prediction method for ignition delay time of liquid spray combustion in constant volume chamber, *Fuel* 287 (2021) 119539.
- [40] S. Xu, S. Zhong, A. Hadadpour, Y. Zhang, K.M. Pang, M. Jangi, H. Fatehi, X.-S. Bai, Large-eddy simulation of the injection timing effects on the dual-fuel spray flame, *Fuel* 310 (2022) 122445.
- [41] L. Valino, A field monte carlo formulation for calculating the probability density function of a single scalar in a turbulent flow, *Flow, TurbulenceCombust.* 60 (2) (1998) 157–172.
- [42] K.M. Pang, M. Jangi, X.-S. Bai, J. Schramm, J.H. Walther, Modelling of diesel spray flames under engine-like conditions using an accelerated Eulerian Stochastic field method, *Combust. Flame* 193 (2018) 363–383.
- [43] C. Dopazo, Relaxation of initial probability density functions in the turbulent convection of scalar fields, *Phys. Fluids* 22 (1) (1979) 20–30.
- [44] W. Jones, A. Marquis, V. Prasad, LES of a turbulent premixed swirl burner using the Eulerian stochastic field method, *Combust. Flame* 159 (10) (2012) 3079–3095.
- [45] H. Pitsch, Flamemaster: A c++ computer program for 0d combustion and 1d laminar flame calculations (1998).

- [46] Y.-S. Niu, L. Vervisch, P.D. Tao, An optimization-based approach to detailed chemistry tabulation: automated progress variable definition, *Combust. Flame* 160 (4) (2013) 776–785.
- [47] R. REITZ, et al., Modeling atomization processes in high-pressure vaporizing sprays, *Atomization and Spray Technology* 3 (4) (1987) 309–337.
- [48] M. Jangi, R. Solsjo, B. Johansson, X.-S. Bai, On large eddy simulation of diesel spray for internal combustion engines, *Int. J. Heat Fluid Flow* 53 (2015) 68–80.
- [49] K.M. Pang, M. Jangi, X.-S. Bai, J. Schramm, Evaluation and optimisation of phenomenological multi-step soot model for spray combustion under diesel engine-like operating conditions, *Combust. Theor. Model.* 19 (3) (2015) 279–308.
- [50] H. Jasak, A. Jemcov, Z. Tukovic, et al., Openfoam: A c++ library for complex physics simulations, *International workshop on coupled methods in numerical dynamics*, volume 1000, IUC Dubrovnik Croatia (2007), pp. 1–20.
- [51] J.C. Ong, K.M. Pang, X.-S. Bai, M. Jangi, J.H. Walther, Large-eddy simulation of n-dodecane spray flame: effects of nozzle diameters on autoignition at varying ambient temperatures, *Proc. Combust. Inst.* 38 (2) (2021) 3427–3434.
- [52] E. Ranzi, A. Frassoldati, A. Stagni, M. Pelucchi, A. Cuoci, T. Faravelli, Reduced kinetic schemes of complex reaction systems: fossil and biomass-derived transportation fuels, *Int. J. Chem. Kinet.* 46 (9) (2014) 512–542.
- [53] Engine combustion network (ECN), <https://ecn.sandia.gov> (accessed 24.02.20) (2015).
- [54] S.A. Skeen, J. Manin, L.M. Pickett, Simultaneous formaldehyde plif and high-speed schlieren imaging for ignition visualization in high-pressure spray flames, *Proc. Combust. Inst.* 35 (3) (2015) 3167–3174.
- [55] J. Abraham, L.M. Pickett, Computed and measured fuel vapor distribution in a diesel spray, *Atomization Sprays* 20 (3) (2010) 241–250.
- [56] Y. Pei, M.J. Davis, L.M. Pickett, S. Som, Engine combustion network (ECN): global sensitivity analysis of spray a for different combustion vessels, *Combust. Flame* 162 (6) (2015) 2337–2347.
- [57] H. Kahila, A. Wehrfritz, O. Kaario, M.G. Masouleh, N. Maes, B. Somers, V. Vuorinen, Large-eddy simulation on the influence of injection pressure in reacting spray a, *Combust. Flame* 191 (2018) 142–159.
- [58] J. Desantes, J. García-Oliver, R. Novella, E. Pérez-Sánchez, Application of a flamelet-based cfd combustion model to the LES simulation of a diesel-like reacting spray, *Comput. Fluids* (2020) 104419.
- [59] M. Ihme, P.C. Ma, L. Bravo, Large eddy simulations of diesel-fuel injection and auto-ignition at transcritical conditions, *Int. J. Engine Res.* 20 (1) (2019) 58–68.
- [60] T. Lucchini, D. Pontoni, G. D'Errico, B. Somers, Modeling diesel combustion with tabulated kinetics and different flame structure assumptions based on flamelet approach, *Int. J. Engine Res.* 21 (1) (2020) 89–100.
- [61] P.C. Ma, H. Wu, T. Jaravel, L. Bravo, M. Ihme, Large-eddy simulations of transcritical injection and auto-ignition using diffuse-interface method and finite-rate chemistry, *Proc. Combust. Inst.* 37 (3) (2019) 3303–3310.
- [62] W.T. Chung, P.C. Ma, M. Ihme, Examination of diesel spray combustion in supercritical ambient fluid using large-eddy simulations, *Int. J. Engine Res.* 21 (1) (2020) 122–133.
- [63] F. Salehi, M. Cleary, A. Masri, Y. Ge, A. Klimenko, Sparse-lagrangian mmc simulations of an n-dodecane jet at engine-relevant conditions, *Proc. Combust. Inst.* 36 (3) (2017) 3577–3585.
- [64] F. Salehi, M. Ghiji, L. Chen, Large eddy simulation of high pressure spray with the focus on injection pressure, *Int. J. Heat Fluid Flow* 82 (2020) 108551.
- [65] A. Wehrfritz, V. Vuorinen, O. Kaario, M. Larmi, Large eddy simulation of high-velocity fuel sprays: studying mesh resolution and breakup model effects for spray a, *Atomization Sprays* 23 (5) (2013) 419–442.
- [66] G. Hindi, E. Paladino, A. de Oliveira Jr, Effect of mesh refinement and model parameters on LES simulation of diesel sprays, *Int. J. Heat Fluid Flow* 71 (2018) 246–259.
- [67] Z. Shi, F. Liu, W. Shang, Y. Li, C. Sun, M. Zhu, Numerical study on the influence of injection pressure on the ignition and combustion of n-dodecane spray at cold-start conditions, *Fuel* 264 (2020) 116882.
- [68] O.T. Kaario, V. Vuorinen, H. Kahila, H.G. Im, M. Larmi, The effect of fuel on high velocity evaporating fuel sprays: large-eddy simulation of spray a with various fuels, *Int. J. Engine Res.* 21 (1) (2020) 26–42.
- [69] F. Payri, J.M. García-Oliver, R. Novella, E.J. Pérez-Sánchez, Influence of the n-dodecane chemical mechanism on the cfd modelling of the diesel-like ECN spray a flame structure at different ambient conditions, *Combust. Flame* 208 (2019) 198–218.
- [70] B. Savard, H. Wang, A. Wehrfritz, E.R. Hawkes, Direct numerical simulations of rich premixed turbulent n-dodecane/air flames at diesel engine conditions, *Proc. Combust. Inst.* 37 (4) (2019) 4655–4662.
- [71] Y. Pei, E.R. Hawkes, M. Bolla, S. Kook, G.M. Goldin, Y. Yang, S.B. Pope, S. Som, An analysis of the structure of an n-dodecane spray flame using tpdf modelling, *Combust. Flame* 168 (2016) 420–435.
- [72] N. Maes, M. Meijer, N. Dam, B. Somers, H.B. Toda, G. Bruneaux, S.A. Skeen, L.M. Pickett, J. Manin, Characterization of spray a flame structure for parametric variations in ecn constant-volume vessels using chemiluminescence and laser-induced fluorescence, *Combust. Flame* 174 (2016) 138–151.
- [73] S.A. Skeen, J. Manin, L.M. Pickett, E. Cenker, G. Bruneaux, K. Kondo, T. Aizawa, F. Westlye, K. Dalen, A. Ivarsson, et al., A progress review on soot experiments and modeling in the engine combustion network (ECN), *SAE Int. J. Engines* 9 (2) (2016) 883–898.
- [74] L.M. Pickett, J. Manin, C.L. Genzale, D.L. Siebers, M.P. Musculus, C.A. Idicheria, Relationship between diesel fuel spray vapor penetration/dispersion and local fuel mixture fraction, *SAE Int. J. Engines* 4 (1) (2011) 764–799.
- [75] P.M. Lillo, L.M. Pickett, H. Persson, O. Andersson, S. Kook, Diesel spray ignition detection and spatial/temporal correction, *SAE Int. J. Engines* 5 (3) (2012) 1330–1346.
- [76] S.A. Skeen, J. Manin, K. Dalen, L.M. Pickett, Extinction-based imaging of soot processes over a range of diesel operating conditions, 8th US National Combustion Meeting (2013), pp. 1–13.
- [77] J. Van Oijen, L. De Goeij, Modelling of premixed laminar flames using flamelet-generated manifolds, *Combust. Sci. Technol.* 161 (1) (2000) 113–137.
- [78] D.O. Lignell, J.H. Chen, H.A. Schmutz, Effects of damköhler number on flame extinction and reignition in turbulent non-premixed flames using DNS, *Combust. Flame* 158 (5) (2011) 949–963.
- [79] N. Maes, The life of a spray, Department of Mechanical Engineering, Eindhoven University of Technology, 2019 Ph.D. thesis.